Check for updates

Multiple resonance type thermally activated delayed fluorescence by dibenzo [1,4] azaborine derivatives

Jaehyun Bae[1,2], Mika Sakai[3], Youichi Tsuchiya[1]*, Naoki Ando[3], Xian-Kai Chen[1], Thanh Ba Nguyen[1,2], Chin-Yiu Chan[1], Yi-Ting Lee[1], Morgan Auffray[1], Hajime Nakanotani[1,2], Shigehiro Yamaguchi[3,4,5]* and Chihaya Adachi[1,2,6]*

[1]Center for Organic Photonics and Electronics Research (OPERA), Kyushu University, Fukuoka, Japan, [2]Department of Chemistry and Biochemistry, Kyushu University, Fukuoka, Japan, [3]Department of Chemistry, Graduate School of Science, Nagoya University, Nagoya, Japan, [4]Research Center for Materials Science (RCMS) and Integrated Research Consortium on Chemical Sciences (IRCCS), Nagoya University, Nagoya, Japan, [5]Institute of Transformative Bio-Molecules (WPI-ITbM), Nagoya University, Nagoya, Japan, [6]International Institute for Carbon Neutral Energy Research (WPI-I²CNER), Kyushu University, Fukuoka, Japan

We studied the photophysical and electroluminescent (EL) characteristics of a series of azaborine derivatives having a pair of boron and nitrogen aimed at the multi-resonance (MR) effect. The computational study with the STEOM-DLPNO-CCSD method clarified that the combination of a BN ring-fusion and a terminal carbazole enhanced the MR effect and spin-orbit coupling matrix element (SOCME), simultaneously. Also, we clarified that the second triplet excited state (T_2) plays an important role in efficient MR-based thermally activated delayed fluorescence (TADF). Furthermore, we obtained a blue−violet OLED with an external EL quantum efficiency (EQE) of 9.1%, implying the presence of a pronounced nonradiative decay path from the lowest triplet excited state (T_1).

KEYWORDS

TADF, thermally activated delayed fluorescence, multi-resonance, azaborine, blue−violet OLED

1 Introduction

Recently, organic emitters providing narrowband emission attracted intense interest aimed at the display applications in organic light-emitting diodes (OLEDs) (Hall et al., 2020; Teng, et al., 2020; Ha et al., 2021; Monkman 2021) because such emitters can achieve high color purity, i.e., high color reproduction area ratio vs. the National Television System Committee (NTSC) color gamut. At the early dawn of OLED development, fluorescence materials had been widely used as an emitter (Tang and VanSlyke, 1987; Adachi et al., 1988; Dodabalapur, 1997; Hung et al., 1997; Shi and Tang., 1997). However, they provide only 25% electron-hole pair-to- photon conversion efficiency because of the
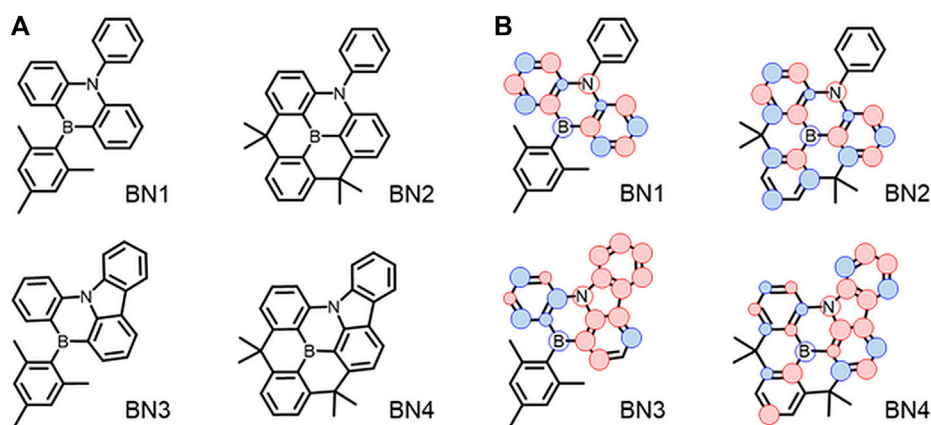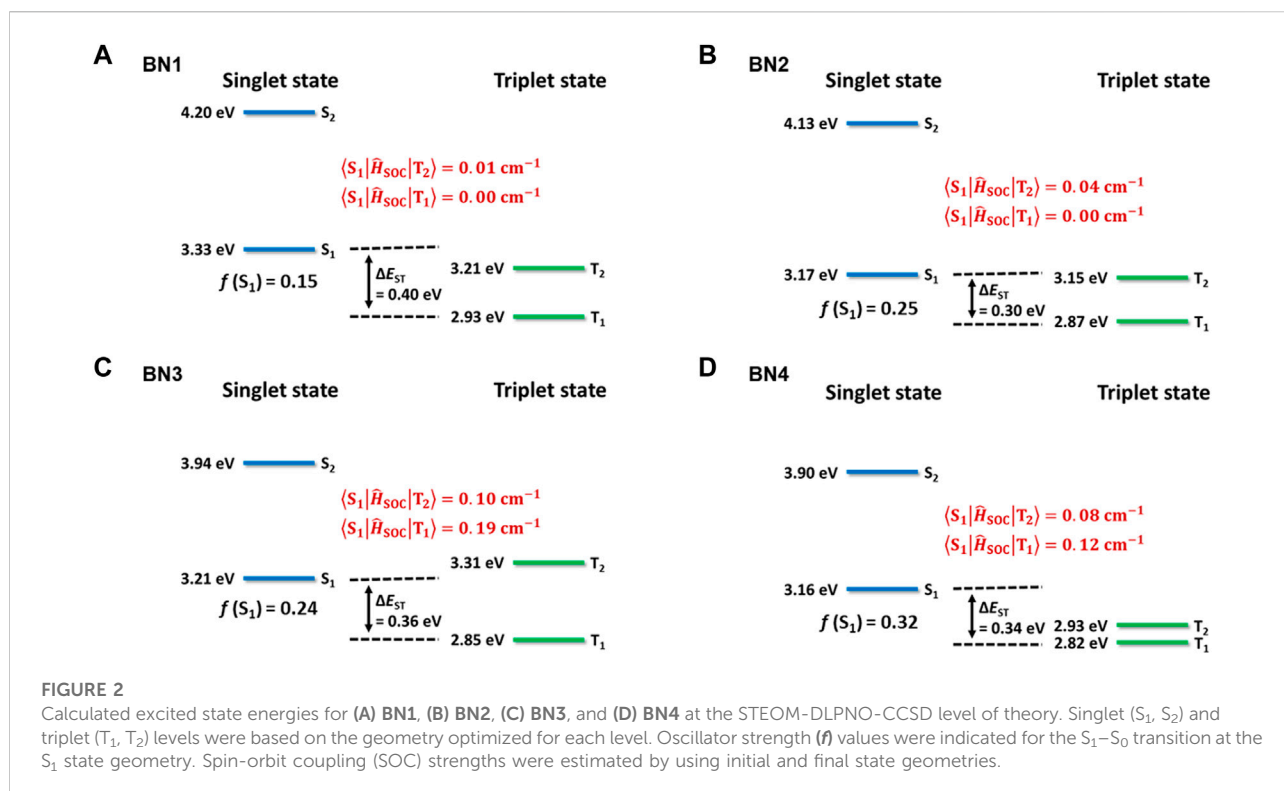
FIGURE 1
(A) Chemical structures of dibenzo [1,4] azaborine derivatives. **(B)** Schematic illustration of the spin density of hole (red) and electron (blue) on main backbone at S_1 state.

spin-statistical theorem (Rothberg and Lovinger, 1996; Köhler et al., 2009). Instead, room temperature phosphorescence materials have resolved this critical problem, achieving 100% internal quantum efficiency (Baldo et al., 1998; Adachi et al., 2001). Nevertheless, the materials had several disadvantages, such as high cost, board emission spectra, and a rather long triplet lifetime, originating from the precious metal complexes and MLCT emission characters. In 2012, on the other hand, our group reported a state-of-the-art emitter based on thermally activated delayed fluorescence (TADF), realizing 100% upconversion from a lowest excited triplet (T_1) to a lowest excited singlet (S_1) using simple aromatic compounds (Uoyama et al., 2012). The TADF emitters can harvest both prompt emission by conventional fluorescence and delayed emission from S_1 *via* reverse intersystem crossing (RISC) from T_1. After this report, a wide variety of TADF materials have been developed worldwide (Nakanotani et al., 2021). However, the TADF emitters also possess the crucial problem of broad emission spectra due to the emission originating from the donor–acceptor (D-A) configuration, i.e., the formation of CT excitons to achieve a small energy splitting between S_1 and T_1 (ΔE_{ST}) (Endo et al., 2009; Endo et al., 2011; Uoyama et al., 2012).

In 2016, Hatakeyama et al. (2016) reported a new type of TADF emitters, achieving narrowband emission with a full width at half maximum (FWHM) of less than 30 nm. These unique emitters were designed by using the MR effects which can localize their highest occupied and lowest unoccupied molecular orbitals (HOMO and LUMO) on the adjacent atoms constituting heterocyclic aromatic cores, achieving unique HOMO and LUMO separation without using the D-A configuration. Also, due to the rigid molecular structures, the vibrational mode of the core structures was significantly suppressed, providing narrowband emission. Furthermore, very recently, a wide

variety of MR-TADF emitters were reported, providing excellent device performance in OLEDs. However, most of the reported MR-TADF emitters have a relatively large ΔE_{ST} compared to the well-elaborated donor–acceptor type TADF emitters, resulting in a small RISC rate ($<10^5$ s^{-1}) while maintaining a large radiative decay rate ($>10^8$ s^{-1}). Therefore, MR-TADF emitters are often used as a terminal emitter in TADF-assisted fluorescence (hyperfluorescence) devices (Nakanotani et al., 2014; Chan et al., 2021). In the recent trend, continuously researchers have been focused on obtaining stable MR-TADF emitters having the compatibility of a narrower FWHM and a large RISC rate by engineering the MR effect to achieve highly stable and high color purity OLEDs (Kondo et al., 2019; Oda et al., 2019).

Previously, we reported the synthesis of MR materials showing narrowband emission with a simple heterocyclic aromatic structure composed of a dibenzo [1,4] azaborine skeleton (**BN1**)-based core having a single couple of boron (B) and nitrogen (N) (Figure 1A) (Ando et al., 2019). This B-N core is the minimum building block to achieve HOMO-LUMO separation on heterocycles rather than the first reported MR-TADF materials of DABNA (Hatakeyama et al., 2016). Based on the scaffold of **BN1**, the ring-fused planar fashion of triarylborane and/or triarylamine to expand the π-conjugation would be expected to improve their photophysical properties (**BN2**, **BN3**, and **BN4**). In this report, we studied the detailed photophysical and OLED characteristics of these emitters. As a result, we found the original azaborine backbone has no TADF property, and the planarization of the *B*- and *N*-phenyl groups by ring-fusion provides the TADF property. Especially, the carbazole formation enhances the SOC, and the most planar **BN4** showed the best TADF characteristics. In addition, it was suggested that the major nonradiative decay of **BN4** occurs from

FIGURE 2
Calculated excited state energies for **(A) BN1**, **(B) BN2**, **(C) BN3**, and **(D) BN4** at the STEOM-DLPNO-CCSD level of theory. Singlet (S_1, S_2) and triplet (T_1, T_2) levels were based on the geometry optimized for each level. Oscillator strength (f) values were indicated for the S_1–S_0 transition at the S_1 state geometry. Spin-orbit coupling (SOC) strengths were estimated by using initial and final state geometries.

the T_1 state because the theoretical EQE has a considerably large difference from the experimental EQE depending on the ratio of two nonradiative decays from S_1 and T_1.

2 Results and discussion

2.1 Computational analysis with wave function-based methodology

First, we performed a theoretical study based on a quantum chemical calculation for **BN1-4**. Recently, Pershin et al. (2019) studied some MR materials, demonstrating the good agreement of ΔE_{ST} between theoretical calculation and experimental values by not using the density functional theory (DFT) method but the wave function-based method with the spin-component scaled (SCS) coupled-cluster model (CC2). While we applied these methods to **BN1-4** at first, the calculation results did not provide a good agreement with the experimental results as shown in the supplemental information (Supplementary Figure S1, Supplementary Table S1). Also, similar to the several reports of MR-TADF emitters (Hatakeyama et al., 2016; Oda et al., 2019; Lee et al., 2021), the DFT calculation with the B3LYP/6-31G(d) level (Stephen et al., 1994) provided a large difference with the experimental results for S_1, T_1 levels, and ΔE_{ST}. In addition, the values of the oscillator strength (f) were inconsistent with the experimentally estimated ones. Next, we

also used the SCS-CC2 level. While it showed better agreement with the experimental ΔE_{ST}, it resulted in lower values when N-phenyl units were incorporated into the fused rings. Moreover, a considerable difference was observed in the energy levels of both singlet and triplet excited states.

With the comprehensive evaluation of the calculation methods, we found the Similarity Transformed Equation-Of-Motion Domain-based Local Pair Natural Orbital Coupled-Cluster Singles and Doubles (STEOM-DLPNO-CCSD) method, which is a wave function-based quantum chemistry approach based on EOM-CCSD (Stephen et al., 1994), provides the best results with the experimental values for S_1, T_1 levels, and ΔE_{ST}. The calculated values of singlet, triplet levels, ΔE_{ST}, spin-orbit coupling matrix element (SOCME), and f are summarized in Figure 2. The hole and electron distributions at the S_1 state for each material are illustrated in Figure 1B. Also, the spin density difference plots for S_1, T_1, and T_2 are shown in Supplementary Figure S2. Because of the higher energy of the S_2 level than that of the S_1, T_1, and T_2 levels, it is reasonable to consider only the lower three levels for the emission process in all **BN**s. Although the absolute f values for the **BN**s' S_1 levels are overestimated, the order is consistent with the π-extension trend of the ring-fused structures. The ΔE_{ST} values, which are also reduced by the π-extension trend, are estimated to be 0.30–0.40 eV, while these values are slightly overestimated, i.e., <0.1 eV, compared to the experimental values. Interestingly, the SOCME showed a large difference for **BN**s, which should be related to the hole and electron distributions at each state of S_1, T_1, and T_2. In the case
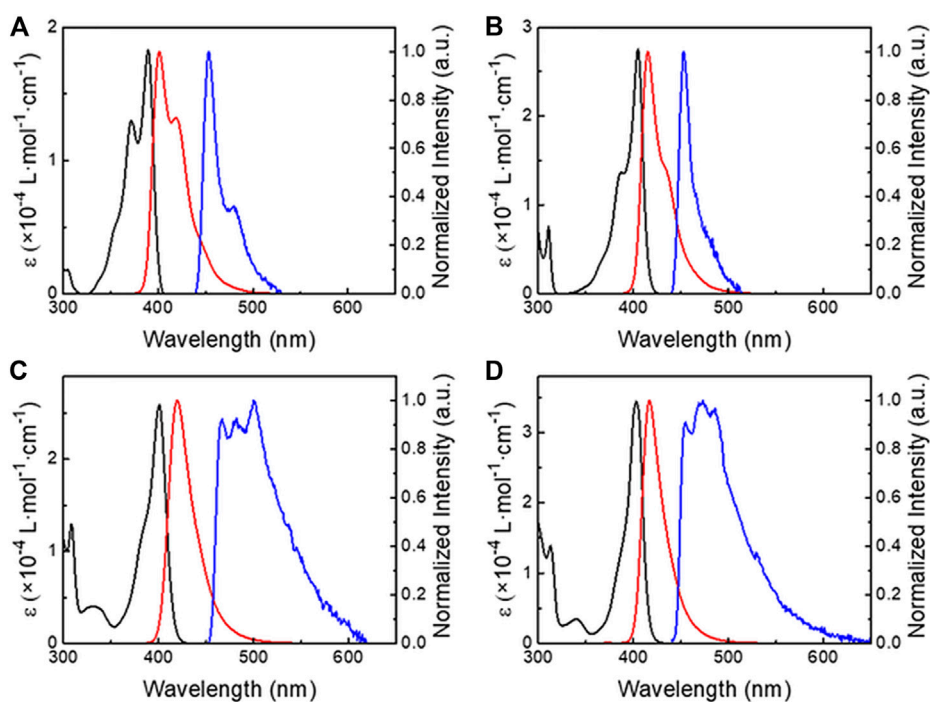
FIGURE 3
Absorption (black line), fluorescence (red line), and phosphorescence (blue line, at 77 K) spectra of **(A) BN1**, **(B) BN2**, **(C) BN3**, **(D) BN4** in toluene $(1.0 \times 10^{-5} \text{ mol L}^{-1})$.

of **BN1** and **BN2**, the SOCMEs between S_1 and T_1 were estimated to be 0.00 cm^{-1} because of the similar hole and electron distributions, which is the forbidden transition explained by El-Sayed's rule. Furthermore, since the SOCMEs between S_1 and T_2 in **BN1** and **BN2** are rather small values of 0.01 and 0.04 cm^{-1}, respectively, they would show virtually no TADF activity. Instead, **BN3** and **BN4** are TADF-active. When an N-phenyl group is fused with the BN ring (**BN3**), the hole distribution of the S_1 state locates mainly on the carbazole moiety, and the electron is distributed on the azaborine moiety, inducing the charge transfer (CT) nature. In the T_1 state, both hole and electrons are distributed on the carbazole moiety, while they distribute on the azaborine moiety in the T_2 state. These spin distribution differences among S_1, T_1, and T_2 enhance the SOCME of **BN3** (0.19 and 0.10 cm^{-1} for S_1-T_1 and S_1-T_2, respectively). In the case of **BN4**, the spin distribution of T_1 is almost as same as **BN3**, while that of the T_2 level spreads to the whole molecule. Interestingly, the SOCME of **BN4** is as same as that with **BN3** (0.12 and 0.08 cm^{-1} for S_1-T_1 and S_1-T_2, respectively).

2.2 Photophysical properties of BN molecule series in solution

Figure 3 shows the ultraviolet–visible (UV–Vis) absorption and emission spectra of **BN1-4** in toluene $(1.0 \times 10^{-5} \text{ mol L}^{-1})$.

Previously, we demonstrated the estimation method of experimental f values for fluorescence materials using the integral of the molar absorption coefficient (ε) which originates from the absorption component located at the lowest energy, and we applied this method to TADF materials (Hirata et al., 2015; Tsuchiya et al., 2020; Tsuchiya et al., 2021a). Also, the transition dipole moment (Q) and radiative decay rate from an S_1 state (k_r^S) can be estimated with the absorption and emission spectra. Fortunately, all four compounds showed the characteristic absorption band at a longer wavelength than ca. 350 nm. Therefore, these absorption bands were separated based on the multi-component Gaussian curve fitting (Supplementary Figure S3). The intense absorption band with a peak around 400 nm can be characterized as a short-range CT transition on the polycyclic aromatic backbone, i.e., the MR nature originated from the fused BN structure. The estimated f, Q, and k_r^S values were provided using the whole lowest absorption band and provided good agreement with the values of computationally estimated f and k_r^S estimated by the transient emission decay and PLQY. The experimental f values were 0.110, 0.129, 0.124, and 0.138 for **BN1**, **2**, **3**, and **4**, respectively (Table 1). This trend showed good agreement with those of the calculated values: 0.15, 0.25, 0.24, and 0.32. The B-phenyl fused **BN2** provides a slightly larger f value than that of N-phenyl fused **BN3** both in the computational and experimental results. The spectroscopic k_r^S

TABLE 1 Photophysical values of BN1-4 in toluene solution (1.0×10^{-5} mol L^{-1}).

Compounds	$\lambda_{abs}{}^{a}$ (nm)	$\varepsilon^{a} \times 10^{-4}$ (L mol^{-1} cm^{-1})	$\lambda_{flu}{}^{b}$ (nm)	PLQY^{c}	FWHM^{a} (nm)	$S_1{}^{d}$ (eV)	$T_1{}^{d}$ (eV)	$E_{ST}{}^{d}$ (eV)	f^{e}	Q^{e} (D)	$k_r{}^{Se}$ (10^{8} s^{-1})
BN1	389	1.83	401	0.98	36	3.20	2.81	0.40	0.110 (0.15)	1.564	1.35 (1.12)
BN2	405	2.75	415	0.98	28	3.08	2.80	0.28	0.129 (0.25)	1.925	1.51 (1.28)
BN3	401	2.59	420	0.86	29	3.09	2.72	0.37	0.124 (0.24)	2.085	1.42 (1.14)
BN4	403	3.44	417	0.86	25	3.09	2.78	0.30	0.138 (0.32)	2.428	1.67 (1.38)

[a]Absorption peak maxima of the lowest energy absorption band.
[b]Emission peak maxima.
[c]Photoluminescence quantum yield measured under inert gas conditions.
[d]S_1 and T_1 are estimated from the onset values of fluorescence and phosphorescence spectra.
[e]Oscillator strength.
(f), Transition dipole moment (Q) and radiative decay rate ($k_r{}^{s}$) are estimated from absorption and emission spectra by the reported method in literature (Tsuchiya et al., 2020). The values of f shown in parentheses are the computationally calculated value with the STEOM-DLPNO-CCSD, level of theory. The values of $k_r{}^{s}$ shown in parentheses are obtained from the emission decay rate and PLQY.

provided ca. 20%–25% large values in all **BN**s compared with the result of transient emission decay measurement in toluene. By comparing those absorption bands, we can recognize that the condensed structures well-suppress the vibronic band in the absorption and fluorescence spectra. Particularly, **BN4** forming the carbazole is the most effective for suppression, and it showed the narrowest band emission with the FWHM of 25 nm (49 meV). The fluorescence spectra of **BN3** have no vibronic structure, but they were slightly broadened compared to those of **BN4** (29 nm). This can be ascribed to the CT-like spin distributions which were found in the theoretical calculation. The expansions of the π-conjugation by planarization also showed a slight bathochromic shift of the absorption and fluorescence spectra; each peak maxima of the absorption spectra for **BN1**, **2**, **3**, and **4** are 389, 405, 401, and 403 nm, respectively. Thus, **BN2** and **BN4** showed a slightly larger bathochromic effect than others.

As expected in the spin distribution on the computational analysis, the *N*-phenyl planarized ones (**BN3** and **4**) showed similar broad phosphorescence spectra having vibronic structures. On the other hand, **BN1** and **2** showed narrowband phosphorescence. The fluorescence and phosphorescence in all **BN**s provided similar spectra in various solvents (Supplementary Figure S4). In other words, **BN**s have less polarity sensitivity for both S_1 and T_1 energies. The estimated S_1, T_1 energy levels, and ΔE_{ST} values in toluene are summarized in Table 1. In addition, the experimentally obtained k_r^{S} also showed good agreement with the estimated k_r^{S} from the spectral data. Unfortunately, it was very difficult to find delayed emission in toluene for all **BN**s. Even the most planar **BN4** showed a very weak delayed emission; $\Phi_{PF} : \Phi_{DF} = 85 : 1$ (Supplementary Figure S5). This would be based on the small

intersystem crossing (ISC) rate ($k_{ISC} = (1.28 \pm 1.09) \times 10^{7}$ s^{-1}) against the sum of radiative and nonradiative decay rates ($k_r^{S} + k_{nr}^{S} = (1.44 \pm 0.11) \times 10^{8}$ s^{-1}) and also the small reverse ISC rate ($k_{RISC} = (9.84 \pm 8.37) \times 10^{4}$ s^{-1}) against the rate of nonradiative decay from T_1 ($k_{nr}^{T} = 1.67 \times 10^{5}$ s^{-1} in maximum). It should be noted that the maximum k_{ISC} and k_{RISC} correspond to the limit condition of $k_{nr}^{T} = 0$ and $k_{nr}^{S} = 0$, respectively. Also, the minimum values correspond to $k_{nr}^{S} = 0$ and $k_{nr}^{T} = 0$, respectively (Tsuchiya et al., 2021b).

2.3 Thermally activated delayed fluorescence properties from the transient decay curve in a DPEPO-doped film

Because all **BN**s would show very weak TADF property in solution, we investigated the photophysical properties of **BN**s in their solid-state films to suppress the nonradiative decays. We used bis [2-(diphenylphosphino) phenyl] ether oxide (DPEPO) as a high T_1 host matrix to confine the high T_1 energy of **BN**s (>2.7 eV). In addition, we fabricated **BN**-doped DPEPO films with a doping ratio of 1 wt% to inhibit the aggregation. The absorption and emission spectra of each **BN** in DPEPO showed almost the same emission spectra as those in toluene (Table 2 and Supplementary Figure S6). Thus, it was confirmed that **BN**s do not aggregate significantly in the doped films. The transient PL properties were investigated by a steak camera system with a fourth harmonic Nd:YAG laser (266 nm) under vacuum (Figure 4 and Supplementary Figure S7).

BNs showed a comparable radiative decay rate ($k_r^{S} = \Phi_{PF}/\tau_p$) with a similar trend to the estimated ones from the spectroscopy, i.e., **BN1** < **BN2** ≈ **BN3** < **BN4** (Table 2). Since

TABLE 2 Estimated photophysical and rate constant values of 1 wt% BNs in the DPEPO doped film.

Doped film	S_1^a (eV)	T_1^a (eV)	ΔE_{ST}^a (eV)	τ_p^b (ns)	τ_d^b (ms)	Φ_{PF}^c	Φ_{DF}^c	Φ_{PLQY}^d	k_r^{Sc} (10^8 s^{-1})	Max. $k_{nr}^{Sc,e}$ (10^7 s^{-1})	Avg. $k_{ISC}^{c,e}$ (10^7 s^{-1})	Avg. $k_{RISC}^{c,e}$ (s^{-1})	Max. $k_{nr}^{Tc,e}$ (s^{-1})
BN1	3.18	2.82	0.36	7.03	—	0.82	—	0.821	1.17	2.55	1.27 ± 1.27	—	—
BN2	3.06	2.78	0.28	5.70	16.24	0.70	0.06	0.762	1.24	3.86	3.25 ± 1.93	41.80 ± 25	49.60
BN3	3.07	2.76	0.29	5.54	13.34	0.67	0.09	0.766	1.21	3.89	4.04 ± 1.95	57.27 ± 28	55.14
BN4	3.07	2.83	0.24	4.96	4.19	0.70	0.10	0.801	1.40	3.49	4.38 ± 1.74	196.50 ± 78	156.51

[a]Estimated from onset values of fluorescence and phosphorescence spectra. $\Delta E_{ST} = S_1 - T_1$.
[b]Prompt and delayed emission lifetimes were estimated from the ns and ms range transient emission decay curves, respectively.
[c]Values were estimated by the reported method in the literature (Tsuchiya et al., 2021b).
[d]Under inert gas conditions.
[e]Maxima values of k_{nr}^S and k_{nr}^T are related to the limited condition of $k_{nr}^T = 0$, and $k_{nr}^S = 0$, respectively. Maximum k_{ISC} and minimum k_{RISC} obtained from average rate constants with the range are relayed to k_{nr}^S and opposite values are related to k_{nr}^T.
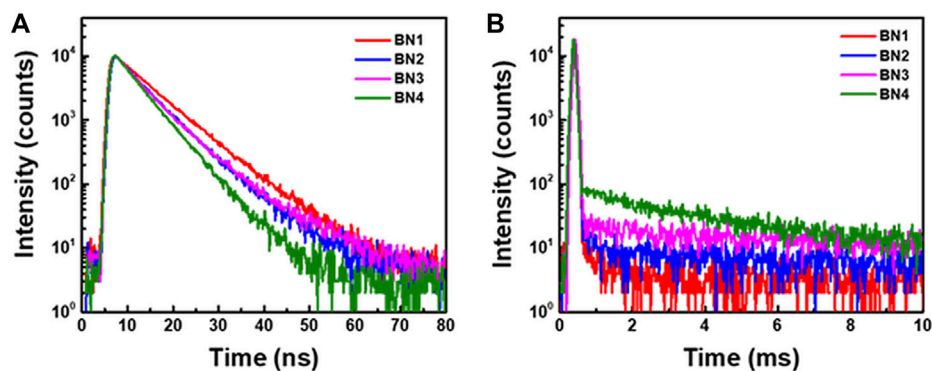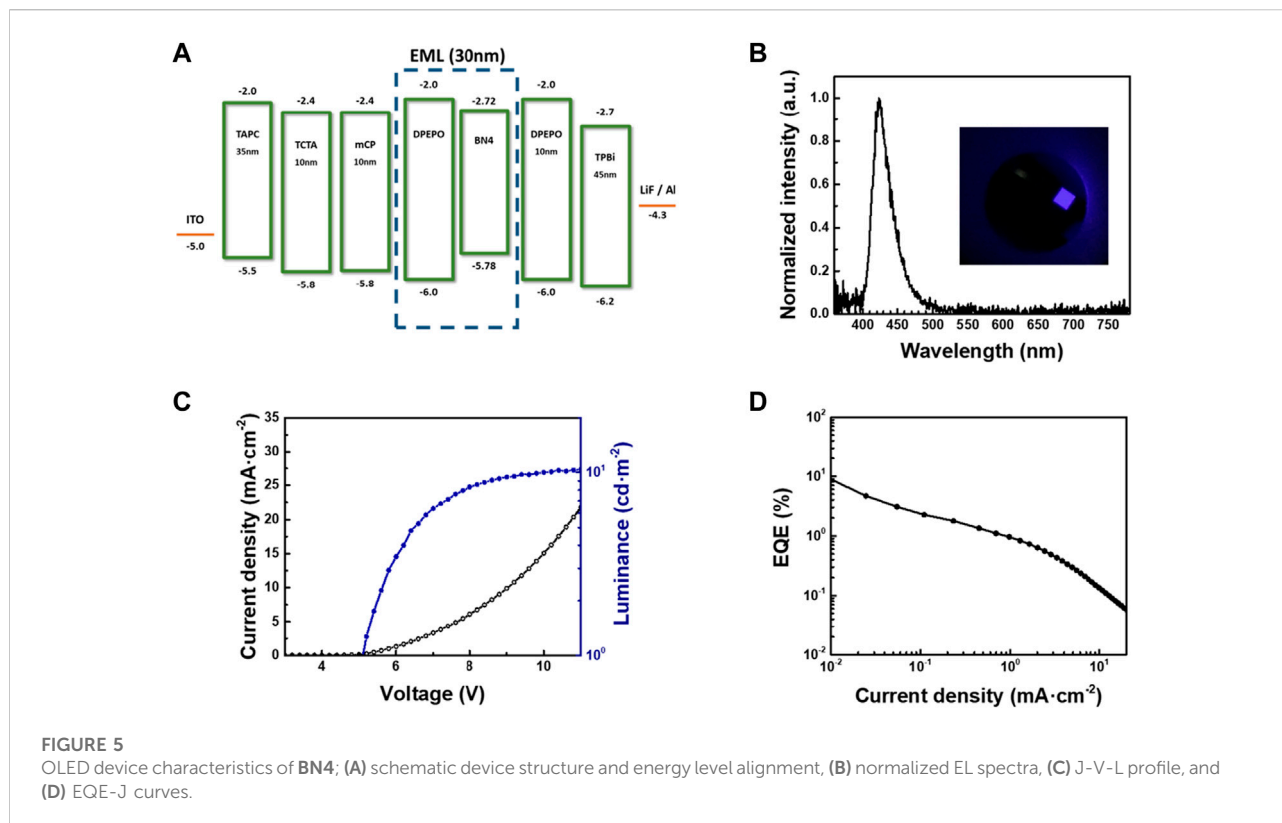

FIGURE 4
Transient PL decay curves of (A) prompt and (B) delayed emissions for BN1, 2, 3, and 4 in DPEPO films (1 wt% doped) were measured with a streak camera under the vacuum at 300 K.

BN1 showed no delayed emission even in the doped film, we conclude that the fundamental dibenzo [1,4] azaborine backbone has no TADF activity. BN1 has a large ΔE_{ST} of 0.36 eV, while other BNs have relatively small ΔE_{ST} of less than 0.30 eV. While the orbital separation of the hole and electron shows a typical MR pattern, it holds a large orbital overlap between them. In addition, BN1 shows a large vibronic structure in its absorption and emission spectra. These results clearly indicate that it is insufficient to achieve MR-TADF by just connecting two phenyl rings to the electron-donating and -withdrawing atoms in the azaborine backbone of BN1. On the other hand, the delayed emission component ratio to the total PLQY was increased by planarization; 0.079, 0.118, and 0.125 for BN2, 3, and 4, respectively. It suggests that the delayed emission is closely related to formation of the carbazole moiety, rather than planarization of the B-phenyl group. Since BN2 has a smaller ΔE_{ST} than BN3,

this result should be originated from the larger SOCME in BN3, which is in good agreement with the computational results (Figure 2). The temperature dependence of transient emission decay profiles of BN1-4 (Supplementary Figure S7A) and those spectra of delayed components (1–10 ms) (Supplementary Figure S7B) clearly explained the BN2-4 has TADF characteristics. BN1 showed the only phosphorescence increase, but BN2-4 showed the decrease of delayed fluorescence, which is carried out by decreasing temperature. All BNs emit in the fluorescence region at 50 K, but this emission would be based on the triplet–triplet annihilation. At 300 K, BN4 showed a much shorter delayed emission lifetime (τ_d = 4.2 ms) than that of BN2 and BN3 (16.2 and 13.3 ms, respectively). It suggests that the T_2 state of BN4 lies at a lower level than that of BN3, leading to efficient upconversion. The k_{ISC} values for BN2, 3, and 4 were estimated to be 1.32×10^7, 2.09×10^7, and 2.64×10^7 s^{-1},

FIGURE 5
OLED device characteristics of **BN4**; **(A)** schematic device structure and energy level alignment, **(B)** normalized EL spectra, **(C)** J-V-L profile, and **(D)** EQE-J curves.

respectively, and k_{RISC} values were 66.8, 85.3, and 204.3 s^{-1}, respectively (at 300 K; it can be approximated to be no phosphorescence in the delayed emission, and this approximation provides $k_{nr}^T = 0$). The possible range for rate constants is summarized in Table 2 (Tsuchiya et al., 2021b). The theoretical k_{RISC} can be estimated by the Marcus equation considering the density of states between T_1 and T_2 (Samanta et al., 2017), and the k_{RISC} s for each RISC pathway was estimated (Supplementary Table S2). Considering the direct RISC process from T_1 to S_1, k_{RISC} **BN3** is slightly larger than that of **BN4**. On the other hand, those values were inverted considering the contribution of a T_2 state ($k_{RISC}^{S_1 \leftarrow T_2 \leftrightarrow T_1}$). When the ΔE_{ST} values obtained from the spectral data were introduced to the Marcus equation with the observed k_{RISC}, the SOCME was estimated to be 0.068 and 0.049 cm^{-1} ($k_{nr}^S = 0$) or 0.115 and 0.075 cm^{-1} ($k_{nr}^T = 0$) for **BN3** and **BN4**, respectively. This trend agreed with the direct RISC process without considering T_2 contribution. Furthermore, the effective SOCME was also estimated with the Marcus plot (Supplementary Figure S8) (Fukuzumi et al., 2015); the detailed estimation method is provided in Supplementary Material S1. The effective SOCMEs of the RISC process for **BN3** and **BN4** were estimated to be ca. 0.0006 and 0.004 cm^{-1}, respectively. In other words, **BN4** provided a larger SOCME which is one order magnitude

larger than that of **BN3** (Supplementary Table S2). Therefore, we concluded the T_n state enhances the RISC process in **BN4**.

2.4 Organic light-emitting diode device employing BN4 as an emitter

Finally, we fabricated an OLED with **BN4** as an emitter (Figure 5) with the device structure of indium tin oxide (ITO)/ 1,1-bis [(di-4-tolylamino) phenyl]cyclohexane (TAPC, 35 nm)/ 4,4′,4″-tris (carbazol-9-yl)-triphenylamine (TCTA, 10 nm)/1,3-bis (9-carbazol-9-yl) benzene (mCP, 10 nm)/DPEPO doped with 1 wt% of **BN4** (30 nm)/DPEPO (10 nm)/2,2′,2″-(1,3,5-benzinetriyl) -tris (1-phenyl-1-*H*-benzimidazole) (TPBi, 45 nm)/LiF (0.8 nm)/Al (100 nm). The electroluminescence spectrum showed good agreement with the PL spectrum of **BN4** in a DPEPO host ($\lambda_{EL,max}$ = 423 nm, FWHM = 31 nm). The CIE coordinates were (0.17, 0.04). The maximum EQE (EQE_{max}) was 9.1%. Here, EQE_{max} can be theoretically estimated with Eq. 1.

$$EQE_{max} = \eta_{int}\eta_{out}\eta_{CB}, \tag{1}$$

where η_{int} is an internal quantum efficiency, η_{out} is an outcoupling efficiency, and η_{CB} is a charge balance factor

(ideally, $\eta_{CB} = 1$). η_{int} can be explained by the emission efficiency from the generated S_1 and T_1 excitons, with the exciton generation efficiency of 1:3 for S_1:T_1. In the case of fluorescence and phosphorescence devices, η_{int} can be explained with effective exciton generation efficiency (η_{exc}) and PLQY (Φ_{PLQY}) as given by Eq. 2.

$$\eta_{int} = \eta_{exc}\Phi_{PLQY} \qquad (2)$$

Recently, this equation has been widely applied to TADF OLEDs since it is reasonable to apply it for highly efficient emitters, i.e., $k_{nr}^S = 0$ or $k_{nr}^T = 0$ (Masui et al., 2013; Dias et al., 2017). However, some TADF molecules possess the nonradiative rates of $k_{nr}^S \neq 0$ or $k_{nr}^T \neq 0$, and we corrected the theoretical equation for η_{int} as Eq. 3 which had been already reported (Endo et al., 2011; Hirata et al., 2015); the derivation is provided in Supplementary Material S1.

$$\eta_{int} = \frac{1}{4}\left(\Phi_{PLQY} + 3\frac{\Phi_{DF}}{\Phi_{ISC}}\right), \qquad (3)$$

where Φ_{ISC} is $k_{ISC}/(k_r^S + k_{nr}^S + k_{ISC})$. The term of Φ_{DF}/Φ_{ISC} becomes Φ_{PLQY} when k_{nr}^T is accurately 0, and it becomes the same as Eq. 2. It should be noted that $\eta_{exc} = 1$ should be considered a maximum value for TADF, meaning that Eq. 2 should not be used when Φ_{PLQY} is not unity. In fact, $k_{nr}^T = 0$ is just a mathematically reasonable value when we can approximate no phosphorescence in emission (Tsuchiya et al., 2021a). When there is the nonradiative path from the T_1 state, it affects 75% of generated triplet excitons by current excitation at first. The ratio of the nonradiative path from a T_1 state in PL is given by $\Phi_{ISC}\Phi_{nr}^T + \sum_{n=1}^{\infty}(\Phi_{ISC}\Phi_{RISC})^n\Phi_{nr}^T$, while that in EL is given by $(0.25\Phi_{ISC} + 0.75)\Phi_{nr}^T + \sum_{n=1}^{\infty}(\Phi_{ISC}\Phi_{RISC})^n\Phi_{nr}^T$ where $\Phi_{nr}^T = k_{nr}^T/(k_r^T + k_{nr}^T + k_{RISC})$. This difference makes $\eta_{int} \neq \Phi_{PLQY}$ for TADF when k_{nr}^T is not 0 accurately. When $\eta_{out} = 0.2$ (which is often employed for the case of the random orientation of molecular alignment of emitters in devices) was employed, the theoretical EQE_{max} for the **BN4** device is calculated as 16.0% and 9.2% for the limit condition of $k_{nr}^T = 0$ and $k_{nr}^S = 0$, respectively. Therefore, it can be concluded that the most of nonradiative decay of **BN4** occurs from the T_1 state in DPEPO.

3 Conclusion

In this study, we focused on the minimum structural component of an azaborine backbone structure, which is necessary to provide MR-TADF characteristics. By planarization with the ring fusion of *B*- or *N*-phenyls, the molecular structure became more rigid, demonstrating clear MR characteristics with suppressing vibronic structures in their spectra. In particular, unlike *B*-phenyl planarization, which reduces FWHM and ΔE_{ST} by simply

extending π-conjugation, it was confirmed that the vibronic structures of emission were suppressed and molecular SOCME was improved through planarization of the *N*-phenyl moiety. Furthermore, we confirmed that the ring fusion of *B*- or *N*-phenyls showed a synergistic effect of them. The TADF nature was mainly dependent on the SOCME because **BN**s showed an appreciably large ΔE_{ST} (0.24–0.36 eV). Carbazole formation enhanced the SOC effectively, and further planarization reduced the T_2 state energy and promoted the RISC process. Finally, we fabricated the OLED having blue–violet emission (λ_{max}, 423 nm) with EQE = 9.1%, demonstrating good agreement with the maximum theoretical value of EQE = 9.2% when the nonradiative decay from the T_1 state is considered. Considering the high PLQY of over 80% in the **BN4** film, it clearly indicates that suppressing the nonradiative process from T_1 is mandatory for efficient MR-TADF OLED in the blue–violet region.

4 Materials and methods

4.1 Chemicals and instruments

All solvents were used as purchased from the Tokyo Chemical Industry (Tokyo, Japan) or Fuji Film-Wako Chemicals (Tokyo, Japan). All synthesis procedures for **BN1**-**4** were provided in the previous report (Ando et al., 2019). Absorption spectra of the samples were measured using an ultraviolet–visible,-near-infrared spectrometer (Lambda 950-PKA, Perkin-Elmer, MA, United States). Fluorescence and phosphorescence spectra were measured using a spectrofluorometer (FP-8600, JASCO International, Japan). The photoluminescence quantum yield (PLQY) was measured using a PLQY measurement system (Quantaurus-QY, Hamamatsu Photonics, Hamamatsu, Japan). The transient PL decay characteristics of **BN4** in toluene were recorded by a dynamic range streak camera system (C10910-01, Hamamatsu Photonics, Hamamatsu, Japan) with a third harmonic YAG laser (355 nm, 10 Hz, PL-2250, EKSPLA, Lithuania) as an excitation source. The transient PL emission and PL decay of **BN1**, **2**, **3**, and **4** doped in a DPEPO host film were recorded under vacuum with a streak camera (C4334, Hamamatsu Photonics, Hamamatsu, Japan) with a third harmonic YAG laser (266 nm, 10 Hz, LS-2132UTF, LOTIS TII, Belarus) as an excitation source.

4.2 Theoretical calculations

The **BN**s were analyzed by DFT calculation with the B3LYP/6-31 + g* (Lee et al., 1988; Beck, 1993) level of theory on Gaussian 16 (Frisch et al., 2016), SCS-CC2 level of theory on TURBOMOLE 7.1.1 (2016), and STEOM-

DLPNO-CCSD level of theory on ORCA 4.2.1 software (Neese et al., 2020).

4.3 Photophysical measurement

The photophysical properties of **BN**s were measured in toluene solution (1.0×10^{-5} mol L^{-1}), which was saturated with inert gas. Also, thermally evaporated films composed of 1 wt% emitter in a DPEPO host were measured under the vacuum condition. The transient PL decay profiles of streak camera measurement were analyzed with the ex-Gauss fitting using Eqs 4, 5; the detailed explanation is written in Supplementary Material S1.

$$I(t) = \sum_{n=1}^{n} \left\{ R_n \left[\sum_{m=1}^{m} I_m \left(t_n, A_m, k_m, \mu_n, \sigma_n \right) \right] \right\}, \quad (4)$$

,

$$I_m \left(t_n, A_m, k_m, \mu_n, \sigma_n \right) = \frac{A_m}{2} \exp\left[\frac{k_m}{2} \left(2\mu_n + k_m\sigma_n^2 \right) \right]$$
$$\mathrm{erfc}\left(\frac{\mu_n + k_m\sigma_n^2 - t_n}{\sqrt{2}\sigma_n} \right) \exp\left(-k_m t_n \right). \quad (5)$$

In this time, $n = 3$ and m $= 2$ were employed to explain three G curves, i.e., probability density functions, as an instrument-related function (IRF) and bi-exponential curve as an emission decay. R_n is the scaling factor for each Gaussian curve to explain IRF and t_n is $t - \mu_n + \mu_1$. A_m and k_m are corresponding to the pre-exponential factor and the decay rate for the bi-exponential curve as an analytical target, respectively. μ_n and σ_n^2 are the terms of the mean and the variance of each Gauss curve, respectively.

Data availability statement

The original contributions presented in the study are included in the article/Supplementary Material; further inquiries can be directed to the corresponding authors.

Author contributions

JB performed the experimental work for photophysics and device fabrication. MK, NA, and SY designed and synthesized the molecules. JB, X-KC, and Y-TL contributed to theoretical calculation. JB, YT, TN, C-YC, MA, and HN contributed to analysis of the data. JB, YT, and CA wrote the manuscript. All authors reviewed the manuscript.

Funding

Conflict of interest

The authors declare that the research was conducted in the absence of any commercial or financial relationships that could be construed as a potential conflict of interest.

The reviewer GX declared a past co-authorship with the author CA to the handling editor.

Publisher's note

All claims expressed in this article are solely those of the authors and do not necessarily represent those of their affiliated organizations, or those of the publisher, the editors, and the reviewers. Any product that may be evaluated in this article, or claim that may be made by its manufacturer, is not guaranteed or endorsed by the publisher.

Supplementary material

The Supplementary Material for this article can be found online at: https://www.frontiersin.org/articles/10.3389/fchem.2022.990918/full#supplementary-material

References

Adachi, C., Baldo, M. A., Thompson, M. E., and Forrest, S. R. (2001). Nearly 100% internal phosphorescence efficiency in an organic light emitting device. *J. Appl. Phys.* 90, 5048–5051. doi:10.1063/1.1409582

Adachi, C., Tokito, S., Tsutsui, T., and Saito, S. (1988). Electroluminescence in organic films with three-layer structure. *Jpn. J. Appl. Phys.* 27, L269–L271. doi:10.1143/JJAP.27.L269

Ando, M., Sakai, M., Ando, N., Hirai, M., and Yamaguchi, S. (2019). Planarized: B, N -phenylated dibenzoazaborine with a carbazole substructure: Electronic impact of the structural constraint. *Org. Biomol. Chem.* 17, 5500–5504. doi:10.1039/c9ob00934e

Baldo, M. A., O'Brien, D. F., You, Y., Shoustikov, A., Sibley, S., Thompson, M. E., et al. (1998). Highly efficient phosphorescent emission from organic electroluminescent devices. *Nature* 395, 151–154. doi:10.1038/25954

Beck, A. D. (1993). Density-functional thermochemistry. III. The role of exact exchange. *J. Chem. Phys.* 98, 5648–5652. doi:10.1063/1.464913

Chan, C. Y., Tanaka, M., Lee, Y. T., Wong, Y. W., Nakanotani, H., Hatakeyama, T., et al. (2021). Stable pure-blue hyperfluorescence organic light-emitting diodes with high-efficiency and narrow emission. *Nat. Photonics* 15, 203–207. doi:10.1038/s41566-020-00745-z

Dias, F. B., Penfold, T. J., and Monkman, A. P. (2017). Photophysics of thermally activated delayed fluorescence molecules. *Methods Appl. Fluoresc.* 5, 012001. doi:10.1088/2050-6120/aa537e

Dodabalapur, A. (1997). Organic light emitting diodes. *Solid State Commun.* 102, 259–267. doi:10.1016/S0038-1098(96)00714-4

Endo, A., Ogasawara, M., Takahashi, A., Yokoyama, D., Kato, Y., and Adachi, C. (2009). Thermally activated delayed fluorescence from Sn4+-porphyrin complexes and their application to organic light-emitting diodes -A novel mechanism for electroluminescence. *Adv. Mat.* 21, 4802–4806. doi:10.1002/adma.200900983

Endo, A., Sato, K., Yoshimura, K., Kai, T., Kawada, A., Miyazaki, H., et al. (2011). Efficient up-conversion of triplet excitons into a singlet state and its application for organic light emitting diodes. *Appl. Phys. Lett.* 98, 083302. doi:10.1063/1.3558906

Frisch, M. J., Trucks, G. W., Schlegel, H. B., Scuseria, G. E., Robb, M. A., Cheeseman, J. R., et al. (2016). *Gaussian 16, revision A.03*. Wallingford CT: Gaussian Inc.

Fukuzumi, S., Itoh, A., Ohkubo, K., and Suenobu, T. (2015). Size-selective incorporation of donor–acceptor linked dyad cations into zeolite Y and long-lived charge separation. *RSC Adv.* 5, 45582–45585. doi:10.1039/c5ra06165b

Ha, J. M., Hur, S. H., Pathak, A., Jeong, J. E., and Woo, H. Y. (2021). Recent advances in organic luminescent materials with narrowband emission. *NPG Asia Mat.* 13, 53. doi:10.1038/s41427-021-00318-8

Hall, D., Suresh, S. M., dos Santos, P. L., Duda, E., Bagnich, S., Pershin, A., et al. (2020). Improving processability and efficiency of resonant TADF emitters: A design strategy. *Adv. Opt. Mat.* 8, 1901627. doi:10.1002/adom.201901627

Hatakeyama, T., Shiren, K., Nakajima, K., Nomura, S., Nakatsuka, S., Kinoshita, K., et al. (2016). Ultrapure blue thermally activated delayed fluorescence molecules: Efficient HOMO-LUMO separation by the multiple resonance effect. *Adv. Mat.* 28, 2777–2781. doi:10.1002/adma.201505491

Hirata, S., Sakai, Y., Masui, K., Tanaka, H., Lee, S. Y., Nomura, H., et al. (2015). Highly efficient blue electroluminescence based on thermally activated delayed fluorescence. *Nat. Mat.* 14, 330–336. doi:10.1038/nmat4154

Hung, L. S., Tang, C. W., and Mason, M. G. (1997). Enhanced electron injection in organic electroluminescence devices using an Al/LiF electrode. *Appl. Phys. Lett.* 70, 152–154. doi:10.1063/1.118344

Kondo, Y., Yoshiura, K., Kitera, S., Nishi, H., Oda, S., Gotoh, H., et al. (2019). Narrowband deep-blue organic light-emitting diode featuring an organoboron-based emitter. *Nat. Photonics* 13, 678–682. doi:10.1038/s41566-019-0476-5

Lee, C., Yang, W., and Parr, R. G. (1988). Development of the Colle-Salvetti correlation-energy formula into a functional of the electron density. *Phys. Rev. B* 37, 785–789. doi:10.1103/PhysRevB.37.785

Lee, Y. T., Chan, C. Y., Tanaka, M., Mamada, M., Balijapalli, U., Tsuchiya, Y., et al. (2021). Investigating HOMO energy levels of terminal emitters for realizing high-brightness and stable TADF-assisted fluorescence organic light-emitting diodes. *Adv. Electron. Mat.* 7, 2001090–2001099. doi:10.1002/aelm.202001090

Masui, K., Nakanotani, H., and Adachi, C. (2013). Analysis of exciton annihilation in high-efficiency sky-blue organic light-emitting diodes with thermally activated delayed fluorescence. *Org. Electron.* 14, 2721–2726. doi:10.1016/j.orgel.2013.07.010

Monkman, A. (2021). Why do we still need a stable long lifetime deep blue OLED emitter? *ACS Appl. Mat. Interfaces* 14, 20463–20467. doi:10.1021/acsami.1c09189

Nakanotani, H., Higuchi, T., Furukawa, T., Masui, K., Morimoto, K., Numata, M., et al. (2014). High-efficiency organic light-emitting diodes with fluorescent emitters. *Nat. Commun.* 5, 4016–4017. doi:10.1038/ncomms5016

Nakanotani, H., Tsuchiya, Y., and Adachi, C. (2021). Thermally-activated delayed fluorescence for light-emitting devices. *Chem. Lett.* 50, 938–948. doi:10.1246/cl.200915

Neese, F., Wennmohs, F., Becker, U., and Riplinger, C. (2020). The ORCA quantum chemistry Program package. *J. Chem. Phys.* 152, 224108. doi:10.1063/5.0004608

Oda, S., Kawakami, B., Kawasumi, R., Okita, R., and Hatakeyama, T. (2019). Multiple resonance effect-induced sky-blue thermally activated delayed fluorescence with a narrow emission band. *Org. Lett.* 21, 9311–9314. doi:10.1021/acs.orglett.9b03342

Pershin, A., Hall, D., Lemaur, V., Sancho-Garcia, J. C., Muccioli, L., Zysman-Colman, E., et al. (2019). Highly emissive excitons with reduced exchange energy in thermally activated delayed fluorescent molecules. *Nat. Commun.* 10, 597–7. doi:10.1038/s41467-019-08495-5

Rothberg, L. J., and Lovinger, A. J. (1996). Status of and prospects for organic electroluminescence. *J. Mat. Res.* 11, 3174–3187. doi:10.1557/JMR.1996.0403

Samanta, P. K., Kim, D., Coropceanu, V., and Brédas, J.-L. (2017). Up-conversion intersystem crossing rates in organic emitters for thermally activated delayed fluorescence: Impact of the nature of singlet vs triplet excited states. *J. Am. Chem. Soc.* 139, 4042–4051. doi:10.1021/jacs.6b12124

Shi, J., and Tang, C. W. (1997). Doped organic electroluminescent devices with improved stability. *Appl. Phys. Lett.* 70, 1665–1667. doi:10.1063/1.118664

Stephen, P. J., Devlin, F. J., Chabalowski, C. F., and Frisch, M. J. (1994). *Ab initio* calculation of vibrational absorption and circular dichroism spectra using density functional force fields. *J. Phys. Chem.* 98, 11623–11627. doi:10.1021/j100096a001

Tang, C. W., and VanSlyke, S. A. (1987). Organic electroluminescent diodes. *Appl. Phys. Lett.* 51, 913–915. doi:10.1063/1.98799

Teng, J. M., Wang, Y. F., and Chen, C. F. (2020). Recent progress of narrowband TADF emitters and their applications in OLEDs. *J. Mat. Chem. C* 8, 11340–11353. doi:10.1039/d0tc02682d

Tsuchiya, Y., Diesing, S., Bencheikh, F., Wada, Y., dos Santos, P. L., Kaji, H., et al. (2021a). Exact solution of kinetic analysis for thermally activated delayed fluorescence materials. *J. Phys. Chem. A* 125, 8074–8089. doi:10.1021/acs.jpca.1c04056

Tsuchiya, Y., Ishikawa, Y., Lee, S. H., Chen, X. K., Brédas, J. L., Nakanotani, H., et al. (2021b). Thermally activated delayed fluorescence properties of trioxoazatriangulene derivatives modified with electron donating groups. *Adv. Opt. Mat.* 9, 2002174–2002178. doi:10.1002/adom.202002174

Tsuchiya, Y., Tsuji, K., Inada, K., Bencheikh, F., Geng, Y., Kwak, H. S., et al. (2020). Molecular design based on donor-weak donor scaffold for blue thermally-activated delayed fluorescence designed by combinatorial DFT calculations. *Front. Chem.* 8, 403–411. doi:10.3389/fchem.2020.00403

Uoyama, H., Goushi, K., Shizu, K., Nomura, H., and Adachi, C. (2012). Highly efficient organic light-emitting diodes from delayed fluorescence. *Nature* 492, 234–238. doi:10.1038/nature11687